

# Impact of Equatorial Wind Stress on Ekman Transport During the Mature Phase of the Indian Ocean Dipole

Linfang Zhang (✉ [1147984953@qq.com](mailto:1147984953@qq.com))

College of Global Change and Earth System Sciences(GCESS),Beijing Normal University,Beijing,100875,China <https://orcid.org/0000-0001-9762-2153>

**Yaokun Li**

College of Global Change and Earth System Sciences(GCESS),Beijing Normal University ,Beijing,100875,China

**Jianping Li**

Laboratory for Ocean Dynamics and Climate,Pilot Qingdao National Laboratory for Marine Sciences and Technology,Qingdao,266237,China

---

## Research Article

**Keywords:** Indian Ocean dipole (IOD), meridional motion, Ekman transport, sea surface temperature anomaly (SSTA)

**Posted Date:** September 13th, 2021

**DOI:** <https://doi.org/10.21203/rs.3.rs-390257/v1>

**License:**  This work is licensed under a Creative Commons Attribution 4.0 International License.

[Read Full License](#)

---

**Version of Record:** A version of this preprint was published at Climate Dynamics on February 21st, 2022. See the published version at <https://doi.org/10.1007/s00382-022-06183-7>.



19

## Abstract

20 This paper investigates the impact of equatorial wind stress on the equatorial  
21 Ekman transport during the Indian Ocean dipole (IOD) mature phase. The results show  
22 that the equatorial zonal wind stress directly drives the meridional motion of seawater  
23 at the upper levels. In normal years, the zonal wind stress south of the equator is easterly  
24 and that north of the equator is westerly, which contributes to southward Ekman  
25 transport at the upper levels to form the climatological Indian Ocean shallow meridional  
26 overturning circulation. During the years of positive IOD events, abnormal easterly  
27 winds near the equator bring southward Ekman transport south of the equator while  
28 they bring northward Ekman transport north of the equator. This causes the seawater to  
29 move away from the equator and hence induces upwelling near the equator, which  
30 forms a pair of small circulation cells that are symmetric about the equator at the upper  
31 levels (approximately 100 m deep). The abnormal circulation cell south (north) of the  
32 equator strengthens (weakens) the southward (northward) motion south (north) of the  
33 equator. During years with negative IOD events, the opposite occurs. In addition,  
34 during the mature period of IOD, the remote sea surface temperature anomaly (SSTA)  
35 such as El Niño–Southern Oscillation (ENSO) may exert some influence on equatorial  
36 wind stress and Ekman transport anomaly but the influence is weak.

37

## 38 **1. Introduction**

39 Ekman transport plays an important role in the meridional overturning circulation  
40 and its associated heat transport in the Indian Ocean. For instance, Lee and Marotzke  
41 (1998) demonstrated that the time-varying Ekman flow of the shallow MOC and its  
42 barotropic compensation can explain most of the seasonal variation of heat transfer in  
43 the IO. Fischer et al. (2002) pointed out that Ekman flow related to mesoscale-  
44 modulated transport is important to the overall upper ocean heat budget in the Arabian  
45 Sea. Hu et al. (2005) calculated the difference between the meridional streamfunction  
46 of the North Indian Ocean (north of 7°S) every year and all the annual mean meridional  
47 streamfunction, and obtained the meridional streamfunction anomaly every year. Then,  
48 the positive and negative typical years were selected for composite analysis. It was  
49 found that the annual mean meridional heat transfer anomalies of the two typical years  
50 showed opposite changes at each latitude.

51 Many studies have shown that the onset and retreat of the Indian Monsoon mainly  
52 promote seasonal cycles of the Ekman transport (Garternicht and Schott 1997; Lee and  
53 Marotzke 1997; Li and Chao 2013). In particular, Lee and Marotzke (1998) concluded  
54 that the maximum seasonal variations of the streamfunction at 10°N and 10°S are  
55 related to monsoon reversal. During the summer monsoon season, westerlies (easterlies)  
56 prevail north (south) of the equator which drive southward Ekman transport in the entire  
57 IO region. During the winter monsoon season, the westerlies change direction to  
58 easterlies which leads to northward Ekman transport in areas north of the equator  
59 (Schott et al. 2002). Additional studies have suggested that the interannual and decadal  
60 changes of the Ekman transport are also linked to corresponding variations in the wind  
61 field. For example, Lee (2004) found that the southeast trade winds over the southern  
62 IO north of approximately 20°S experienced a near-decadal (1992–2000) weakening so

63 the strength of the Ekman transport controlled by these winds diminished during this  
64 period. In contrast, the southwesterlies over the northern IO showed little decadal  
65 change during this period and hence, the Ekman transport related to the cross-equatorial  
66 cell remained relatively steady.

67 In terms of wind variations in the IO, some studies have found that during an  
68 Indian Ocean dipole (IOD) event, the surface wind field over the tropical IO varies  
69 greatly, especially its zonal component (Li et al. 2003; Webster et al. 1999; Zhang et al.  
70 2018). This fact indicates that wind anomalies accompanying the IOD may play a vital  
71 role in controlling the corresponding equatorial Ekman transport. However, few studies  
72 have been conducted to address the relationship between wind anomalies over the  
73 equator and the Ekman transport. Wang et al. (2014) decomposed the deep MOC  
74 (DMOC) in the IO into Ekman and geostrophic transport, external mode and a residual  
75 term. They found that each dynamic component plays a different role in different stages  
76 of the IOD and that the changes of relative contributions of each component are related  
77 to SST and wind anomalies, which are related to the IOD. Their main focus was the  
78 deep thermohaline circulation and the Ekman layer was not discussed. Sherin et al.  
79 (2018) pointed out that wind anomalies during IOD events may affect variations in the  
80 East India Coastal Current (EICC) and that abnormal northward (southward) transport  
81 may occur in the winter during positive (negative) IOD events, usually up to 5 Sv (7  
82 Sv). They emphasized the influence of the IOD on coastal currents and did not focus  
83 on the equatorial Ekman transport. Therefore, the impact of the wind field during IOD  
84 peak periods on the equatorial Ekman transport is still unclear and needs further  
85 investigation.

86 This paper aims to deal with this unsolved question and proposes a physical  
87 mechanism by which surface winds affect the equatorial Ekman transport during the

88 IOD mature period. The remainder of this paper is organized as follows: section 2  
89 describes the data and methodology used in the study; section 3 presents the statistical  
90 relationships between equatorial wind stress and the Ekman transport during the IOD  
91 mature phase and section 4 investigates the possible physical mechanisms; section 5  
92 discusses the influence of ENSO; and section 6 summarizes the findings.

## 93 **2. Data and methodology**

94 The Simple Ocean Data Assimilation (SODA) version 2.1.6 product is used to  
95 calculate the shallow streamfunction in the IO. SODA version 2.1.6 has a horizontal  
96 resolution of  $0.5^{\circ} \times 0.5^{\circ}$  and vertical resolution of 40 levels which extend from near the  
97 surface to a depth of 5,000 meters with a nonuniform distribution. These data cover the  
98 time span from January 1958 to December 2008. The physical variables include  
99 temperature, salinity, velocity, and wind stress. SODA assimilates a large amount of  
100 observational data (Carton et al. 2000) and is an important data source for ocean  
101 research (Schott et al. 2002; Xie et al. 2002).

102 The stream function of MOC in the IO is calculated by

$$103 \quad \psi(\varphi, z) = a \int_{\lambda_w}^{\lambda_e} \int_{z_s}^z v(\lambda, \varphi, z) \cos \varphi \, dz d\lambda, \quad (1)$$

104 where  $\lambda$ ,  $\varphi$ ,  $z$  are the longitude, latitude, and depth, respectively;  $\lambda_w$ ,  $\lambda_e$  are the  
105 western and eastern coasts of the IO, respectively;  $z_s$  is the topography; and  $a$  is the  
106 Earth's radius. Since we mainly discuss the wind-driven Ekman transport, we only  
107 analyzed the stream function in the upper 500 meters. It is found that the circulation  
108 anomaly caused by equatorial wind stress mainly occurs in the Ekman layer near the  
109 equator during the IOD mature period. So EETAI (equatorial Ekman transport anomaly  
110 intensity) is represented by the maximum value of circulation anomaly caused by  
111 equatorial wind stress during the mature period of IOD.

112 The Ekman transport in the IO is calculated by

$$U_E \equiv \int_{-D_E}^0 u dz = \frac{1}{\rho_o f} \tau^y \quad (2)$$

$$V_E \equiv \int_{-D_E}^0 v dz = -\frac{1}{\rho_o f} \tau^x \quad (3)$$

118 Where  $U_E$  is the zonal Ekman transport,  $V_E$  is the meridional Ekman transport, and  
 119  $D_E$  represents the thickness of Ekman layer, which is about tens of meters to more than  
 120 100 meters in the tropical ocean (Stewart, 2004).  $u$  is the zonal velocity of sea water,  
 121  $v$  is the meridional velocity of sea water,  $\rho_o$  represents the density of sea water and the  
 122 average value is  $1025\text{kg}\cdot\text{m}^{-3}$ ,  $f$  is the Coriolis coefficient, and  $\tau^y$  and  $\tau^x$  are the  
 123 meridional wind stress and zonal wind stress. Ekman layer transport is the transport of  
 124 the sea surface boundary layer directly driven by the wind stress. Its direction is  
 125 perpendicular to the wind stress (it points to the right of the wind stress in the northern  
 126 hemisphere and to the left of the wind stress in the southern hemisphere). Its magnitude  
 127 is related to the wind stress intensity and latitude.

128 The spatial variation of wind stress (and the variation of Coriolis parameters with  
 129 latitude) can cause the spatial variation of Ekman layer transport, which leads to  
 130 convergence, divergence and corresponding upward and downward motion, which is  
 131 called Ekman pumping. The Ekman pumping in the IO is calculated by

$$w|_{z=-D_E} = \frac{\partial}{\partial x} \left( \frac{\tau^y}{\rho_o f} \right) - \frac{\partial}{\partial y} \left( \frac{\tau^x}{\rho_o f} \right) \quad (4)$$

133 Where  $\rho_o$  is the density of sea water, with an average value of  $1025\text{kg}\cdot\text{m}^{-3}$ ,  $f$  is the  
 134 Coriolis coefficient, and  $\tau^y$  and  $\tau^x$  are the meridional and latitudinal wind stress.

135 The Sverdrup transport in the IO is calculated by

$$V_y = \frac{1}{\beta \rho_o} \left( \frac{\partial \tau^y}{\partial x} - \frac{\partial \tau^x}{\partial y} \right) \quad (5)$$

137 Where  $V_y$  is the integral of the North-South volume transport from the sea surface to

138 the motionless depth (the vertical range exceeds the depth of Ekman layer, which is  
 139 called "wind-driven circulation layer"), which is called Sverdrup transport.  $\rho_0$  is the  
 140 density of sea water, with an average value of  $1025\text{kg}\cdot\text{m}^{-3}$ ,  $\beta$  is the change rate of  
 141 Coriolis coefficient with latitude, and  $\tau^y$  and  $\tau^x$  are the meridional and latitudinal  
 142 wind stress.

143 We applied the Hadley center SST dataset (Rayner et al. 2003) to calculate the  
 144 Dipole Mode Index (DMI), which was defined as the difference in SST anomalies  
 145 between the west pole ( $50^\circ\text{--}70^\circ\text{E}$ ,  $10^\circ\text{S--}10^\circ\text{N}$ ) and east pole ( $90^\circ\text{--}110^\circ\text{E}$ ,  $10^\circ\text{S--}0^\circ$ ) by  
 146 Saji et al. (1999). Based on the threshold of 1.0 from the standardized SON DMI time  
 147 series, we select the positive phase years ( $>1$ ) of IOD, and based on the threshold of  
 148 -1, we choose the negative phase years ( $<-1$ ) of IOD, respectively. The Niño-3.4 index,  
 149 which is calculated from the area-averaged SSTAs over the equatorial central Pacific  
 150 ( $5^\circ\text{S--}5^\circ\text{N}$ ,  $120^\circ\text{--}170^\circ\text{W}$ ) by the Climate Prediction Center (CPC) using National  
 151 Oceanic and Atmospheric Administration (NOAA) ERSST V5 data (Huang et al. 2017),  
 152 is used to describe ENSO. The statistical diagnosis methods used include correlation  
 153 coefficients and composite differences. The statistical significance of the results was  
 154 determined by the Student's t test.

155 The partial regression coefficient is written as (Jiang and Li 2019):

$$156 \quad C_{Y(B|A)} = \frac{R_{YB} - R_{YA} * R_{AB}}{\sqrt{1 - R_{AB}^2}} * \frac{S_Y}{S_{B|A}} \quad (5)$$

157 Where is  $Y$  represents the regression variable streamfunction,  $B$  represents the zonal  
 158 wind stress in the box in figure 2, and  $A$  is Niño-3.4 index that is proposed to remove.

159 The term  $C_{Y(B|A)}$  is the partial regression coefficient between streamfunction  $Y$  and

160 zonal wind stress  $B$  after the influence of Niño-3.4 index  $A$  is removed from  $B$ .  $R_{YB}$   
161 denotes the correlation coefficient of streamfunction  $Y$  and zonal wind stress  $B$ ;  $R_{YA}$   
162 is the correlation coefficient of streamfunction  $Y$  and Niño-3.4 index  $A$ ;  $R_{AB}$  is the  
163 correlation coefficient of Niño-3.4 index  $A$  and zonal wind stress  $B$ .  $S_Y$ ,  $S_{B|A}$  in the  
164 equation denotes the standard deviation of streamfunction  $Y$  and the standard  
165 deviation of zonal wind stress  $B$  after removing Niño-3.4 index  $A$ .

### 166 **3. Relationship between wind stress and equatorial Ekman transport**

167 The IOD is closely related to the equatorial zonal wind in the IO. According to  
168 Saji et al. (1999) and Wang et al. (2014), the cold SSTAs, which accompany the nearby  
169 southeasterly wind anomaly, first appear in the southeast tropical IO from May to June  
170 (Fig. 1a). In the following months, the cold SSTAs intensify and expand along the  
171 Indonesian coastline to the equator while the western tropical IO begins to warm which  
172 is consistent with the increasing zonal winds along the equator and in Sumatra's coastal  
173 region (Fig. 1b). A sharp peak of these characteristics occurs in October and then  
174 quickly subsides (Fig. 1c, d). Since this relationship reaches its peak in autumn, we  
175 show the correlation coefficient distributions of the September-October-November  
176 (SON) DMI with SST and wind stress in the IO (Fig. 2). The spatial structure of the  
177 correlation between SON DMI and SST features a typical IOD pattern with significant  
178 negative correlation coefficients off the coast of Indonesia and significant positive  
179 correlation coefficients in the central and western Indian Ocean (shaded in Fig. 2).  
180 Meanwhile, the significant easterly anomalies which prevail in the central and eastern  
181 tropical IO suggest a tightly coupled relationship between the IOD and zonal wind

182 stress (vectors in Fig. 2). To further characterize this relationship, a zonal wind stress  
183 index (ZWI) is defined by calculating the average zonal wind stress within a box (e.g.,  
184  $10^{\circ}$  S- $10^{\circ}$  N,  $70^{\circ}$  E- $97^{\circ}$  E) where the most significant easterly anomalies prevail. It  
185 is obvious that the time series of DMI and ZWI (see in Fig. 3b) are highly correlated  
186 (the correlation coefficients reach as high as -0.81 and exceeding the 99% significance  
187 level).

188         Considering the driving effect of the zonal wind stress on the equatorial Ekman  
189 transport, Fig. 3a shows the seasonal correlations between the ZWI and the EETAI.  
190 Based on these results, the ZWI is most significantly correlated with the EETAI during  
191 the autumn season (correlation coefficient is 0.82), while the zonal wind stress shows  
192 certain relationships on the EETA in other seasons.

193         Fig. 4 further shows spatial correlation map between the ZWI and shallow  
194 streamfunction in the autumn. The correlations show a certain symmetry about the  
195 equator but with generally opposite distributions in the upper and deep levels. At depths  
196 of approximately 100 meters, the region between  $10^{\circ}$ S- $0^{\circ}$  exhibits significant positive  
197 correlations while the northern IO region between  $0^{\circ}$ -  $25^{\circ}$  N shows significant negative  
198 correlations. At depths greater 100 meters, the positive and negative correlations switch  
199 their locations.

200         The above analysis suggests that there is a close statistical relationship between  
201 the zonal wind stress during the IOD mature period and equatorial Ekman transport for  
202 both time series and spatial patterns. In the following section, we further explore the  
203 physical mechanisms that equatorial zonal wind stress variations associated with the  
204 IOD mature phase could drive the corresponding equatorial Ekman transport variations.

## 205 **4. Impact of equatorial zonal wind stress on the equatorial Ekman transport**

### 206 *a. Volume transport induced by wind stress*

207 The equatorial wind stress in the mature phase of IOD can drive Ekman transport  
208 which has a direct impact on the shallow MOC. Fig. 5a presents a correlation map of  
209 the ZWI with Ekman transport (vectors) and Ekman pumping (shading) calculated from  
210 the wind stress in the SON. We do not portray Ekman transport near the equator (5°S-  
211 5°N) since it is undefined at the equator. As shown in the figure, the westerly wind  
212 stress anomalies are statistically associated with southward Ekman transport at the  
213 northern IO while they are statistically associated northward Ekman transport from  
214 10°S to the equator. This indicates downward Ekman pumping due to seawater  
215 convergence near the equator. However, away from the equator, accelerating southward  
216 Ekman transport north of the equator leads to seawater divergence and hence upward  
217 Ekman pumping. The same upward Ekman pumping south of the equator extends to  
218 approximately 15°S. It is clear that downward seawater motion near the equator and  
219 upward motions adjacent to downward motions will form two meridional cells which  
220 are symmetric about the equator in the Ekman layer. This implies that when easterly  
221 anomalies prevail near the equator, they can drive two anomalous meridional cells in  
222 the tropical IO. Since Ekman transport is not defined at the equator, we use Ekman  
223 transport difference between 5°S and 5°N to represent cross-equatorial Ekman transport  
224 (CEET). A comparison of SON ZWI (SON DMI) and the CEET shows that the  
225 correlation coefficient reaches 0.98 (-0.77), which is beyond the 99% confidence level  
226 (Fig.5b). This indicates that when the DMI grows, the easterly is enhanced and the  
227 southward Ekman transport increases (value decreases) in autumn, and on the contrary,  
228 it weakens.

229 To further demonstrate the physical linkage between equatorial wind stress and

230 Ekman transport in the tropical IO, Fig. 6 presents composites of Ekman transport and  
231 Ekman pumping that equatorial wind stress drives in both the positive and negative  
232 IOD phases. The easterly wind stress anomalies in the positive IOD phase (Fig. 6a)  
233 induce northward (southward) Ekman transport north (south) of the equator. More  
234 specifically, northward and southward Ekman transports mainly occur in the eastern IO  
235 which indicates the more significant wind stress anomalies in the eastern IO. The off-  
236 equatorial Ekman transport induces upwelling near the equator and the weakened  
237 Ekman transport apart from the equator accompany with the downwelling there. As a  
238 result, two meridional cells that share the same upwelling near the equator form in the  
239 Ekman layer. The situation during negative IOD phases is just the opposite in the  
240 equatorial eastern IO, but the intensity is weaker than that in the positive IOD phase. In  
241 the equatorial eastern IO, the westerly wind stress anomalies initiate southward  
242 (northward) Ekman transport north (south) of the equator. The enhanced Ekman  
243 transport to the equator leads to the downwelling at the equator and the upwelling  
244 outside the equator (Fig. 6b).

245 Above analysis suggests that wind stress anomalies can drive the corresponding  
246 motions in the Ekman layer. Wind stress can also drive the motions in the thermocline  
247 layer. Therefore, we calculated the differences between Sverdrup transport and Ekman  
248 transport, which represents transport in the thermocline layer, to identify the indirect  
249 influence of wind stress. From a zonally averaged perspective, transport in the  
250 thermocline layer is in the opposite direction compared to the Ekman layer above it  
251 (Fig. 7). In a positive IOD phase (Fig. 7a), the off-equatorial Ekman transport must be  
252 balanced by the in-equatorial transport in the thermocline layer. This suggests that the  
253 shallow MOC will exhibit opposite anomalies in the Ekman layer relative to the  
254 thermocline layer (Fig. 7c). In a negative IOD phase (Fig. 7b, d), this situation is similar

255 except for the weakened transport anomalies and shallow MOC anomalies.

### 256 *b. Surface ocean currents induced by the zonal wind stress*

257 We use the velocity at 5 m depth to represent the surface ocean current; Fig. 8  
258 presents a map of the correlations of ZWI with surface ocean currents in autumn. Fig.  
259 8 shows that there is a significant positive correlation between the ZWI and the  
260 Southwest Monsoon Current (SMC), which is caused by the southwest monsoon at 5°  
261 S-5° N in the east-west direction, which indicates that when the westerly anomaly  
262 occurs, the SMC increases.

263 Fig. 9 shows surface ocean current anomalies in a positive phase year and negative  
264 phase year for the IOD. In the positive phase year for the IOD, the SMC is weakened  
265 because there is a clear westward flow anomaly between 5°S-5°N. However, the  
266 difference is that there is a southward flow phenomenon in the southern ocean current  
267 anomaly near the equator while the northward flow is located north of the equator (Fig.  
268 9a). In the negative phase year for the IOD, the SMC in the central to eastern basin is  
269 strengthened due to a weak eastward flow anomaly while the SMC to the west is  
270 weakened due to the weak westward flow anomaly and there is a northward flow  
271 anomaly between 5° S-0°. In general, surface ocean current anomalies for IOD negative  
272 phase years are less robust than those for IOD positive phase years (Fig. 9b).

## 273 **5. Summary and discussion**

274 This paper investigates the influence of equatorial wind stress on the equatorial  
275 Ekman transport during IOD mature phases by analyzing the SODA dataset. The main  
276 findings are as follows. The wind stress associated with IOD mature phases can modify  
277 transport in the Ekman layer and thermocline layer which can lead to corresponding  
278 upwelling and downwelling.

279 In the positive phase of the IOD, cold SSTAs are present along the coasts of

280 Sumatra and Java, warm SSTAs are present along the East African coast, and there is a  
281 southeast wind anomaly near the equator ( $10^{\circ}$  S- $10^{\circ}$  N). Therefore, the surface layer  
282 flows south in the south of the equator, sinks at  $10^{\circ}$ S, reaches 100 m depth, then turns  
283 back to the north, rises at the equator, and forms a counterclockwise circulation. In  
284 contrast, the anomaly for meridional (Ekman) transport is present northward from  $0^{\circ}$  to  
285  $5^{\circ}$ N, sinks at  $5^{\circ}$ N, reaches 60 m depth, turns southward and ascends at the equator to  
286 form a clockwise circulation. As a consequence, there are two small circulation  
287 anomalies with equatorial symmetry at 100m depths and the transport below 100 meters  
288 displays opposite characteristics (Fig. 11).

289 In contrast, in the negative phase of an IOD warm SSTAs are present in the  
290 southeast part of the Indian Ocean, cold SSTAs are present in the west, and a westerly  
291 anomaly exists near the equator. As a result, the corresponding surface transport  
292 anomaly is northward in the south of the equator, descends at the equator, reaches 60 m  
293 depth, turns back to the south, goes up at  $5^{\circ}$ S, and forms a clockwise circulation.  
294 Conversely, the Ekman transport anomaly located north of the equator is southward,  
295 descends at the equator, reaches 200 m depth, and then returns northward and rises at  
296  $10^{\circ}$ N to form an anticlockwise circulation. Thus, there are two small circulation  
297 anomalies that are symmetric about the equator at a depth of 100 m, the equator is a  
298 sinking current, and the transport below 100 m is the opposite. Furthermore, the  
299 anomalies in wind stress and stream function during IOD mature periods exhibit phase  
300 asymmetry, i.e., positive phase years are greater than negative phase years.

301 For IOD formation, one factor is the internal variability of the Indian Ocean and  
302 the other factor is external El Niño–Southern Oscillation (ENSO) forcing (Ashok et al.  
303 2003; Behera et al. 2006; Yang et al. 2015; Zhang et al. 2019). Hence, it is important  
304 to assess the influence of ENSO on the relationship between the EETAI and equatorial

305 wind stress during IOD mature periods. For this purpose, Table 1 shows the partial  
306 correlation of the EETAI with equatorial wind stress and SON DMI after removal of  
307 the preceding DJF, MAM, JJA and SON ENSO signals for the period from 1958 to  
308 2008. The correlation coefficient between the equatorial wind stress and EETAI is 0.82  
309 while this decreases to 0.69 (still significant at the 99% level) after removal of the SON1  
310 ENSO signal; i.e., it barely changes even after removing the signals of the preceding  
311 DJF1, MAM1, JJA1 and D1JF2 ENSO signals. Except for the equatorial wind stress,  
312 the partial correlation coefficients between the SON DMI and EETAI are still significant  
313 after removal of the preceding DJF1, MAM1, JJA1, SON1 and D1JF2 ENSO signals  
314 (Table 1). These results indicate that the equatorial wind stress is significantly correlated  
315 with the EETAI in SON, although ENSO can slightly weaken their relationship. In  
316 addition, we regress the shallow streamfunction on the ZWI both under the condition  
317 of the regular and ENSO independent indices (Fig. 10). The regression coefficient  
318 within 100 meters near the equator did not change much after removal of the SON1,  
319 D1JF2 ENSO signals, which indicates that ENSO has little effect on the relationship of  
320 equatorial wind stress and Ekman transport during the IOD mature period. This shows  
321 that ENSO may exert some influence on equatorial wind stress and Ekman transport in  
322 the year of the IOD events, but the influence is weak.

323

324

325

326

327

328

329

330

331 **Acknowledgements**

332       We are very grateful to NOAA for providing GHCN CAMS and (NCEP/NCAR)  
333 reanalysis data (1948-2017). This study was funded jointly by the National Natural  
334 Science Foundation of China (Grants 41505042, 41805041); the National Program on  
335 Global Change and Air–Sea Interaction (GASI-IPOVAI-03); the National Basis  
336 Research Program of China (2015CB953601, 2014CB953903); and the Fundamental  
337 Research Funds for the Central Universities.

338

339

340

341

342

343

344

345

346

347

348

349

350

351

352

353

354

355

356

357

358

## References

359 Ashok K, Guan ZY, Yamagata T (2003) A Look at the Relationship between the ENSO  
360 and the Indian Ocean Dipole. *Journal of the Meteorological Society of Japan. Ser. II*  
361 81(1):41-56.

362 Behera SK, Luo JJ, Masson S, Rao SA, Sakuma H, Yamagata T (2006) A CGCM Study  
363 on the Interaction between IOD and ENSO. *J Climate* 19(9):1688-1705.

364 Carton JA, Chepurin G, Cao XH (2000) A Simple Ocean Data Assimilation Analysis  
365 of the Global Upper Ocean 1950–95. Part II: Results. *J Phys Oceanogr* 30(2):311-326.

366 Fischer AS, Weller RA, Rudnick DL, Eriksen CC, Lee CM, Brink KH, Fox CA, Leben  
367 RR (2002) Mesoscale eddies, coastal upwelling, and the upper-ocean heat budget in the  
368 Arabian Sea. *Deep-Sea Research II* 49(12):2231-2264.

369 Garternicht U, Schott F (1997) Heat fluxes of the Indian Ocean from a global eddy -  
370 resolving model. *J Geophys Res Oceans* 102(C9):21147-21159.

371 Huang B, Thorne PW, Banzon VF, Boyer T, Zhang HM (2017) Extended  
372 Reconstructed Sea Surface Temperature, Version 5 (ERSSTv5): Upgrades, Validations,  
373 and Intercomparisons. *J Climate* 30(20):8179-8205.

374 Hu RJ, Liu QY, Wu S (2005) Interannual variation of the North Indian Ocean cross  
375 equatorial meridional overturning circulation. *Periodical of Ocean University of China*  
376 (Natural Science Edition) 35 (005): 697-702.

377 Jiang LS, Li T (2019) Relative roles of El Niño-induced extratropical and tropical  
378 forcing in generating Tropical North Atlantic (TNA) SST anomaly. *Clim*

379 Dynam 53: 3791–3804.

380 Lee T (2004) Decadal weakening of the shallow overturning circulation in the South  
381 Indian Ocean. *Geophys Res Lett* 31(18):L18305.

382 Lee T, Marotzke J (1997) Inferring meridional mass and heat transports of the Indian  
383 Ocean by fitting a general circulation model to climatological data. *J Geophys Res*  
384 *Oceans* 102(C5):10585-10602.

385 Lee T, Marotzke J (1998) Seasonal Cycles of Meridional Overturning and Heat  
386 Transport of the Indian Ocean. *J Phys Oceanogr* 28(5):923-943.

387 Li YK, Chao JP (2013) Structure of the Indian Ocean Meridional Overturning  
388 Circulation and its relationship with the zonal wind stress. *Scientia Sinica (Terrae)*  
389 43(10):1708-1716.

390 Li T, Wang B, Chang CP, Zhang YS (2003) A Theory for the Indian Ocean Dipole–  
391 Zonal Mode. *J Atmos Sci* 60(17):2119-2135.

392 Rayner NA, Parker DE, Horton EB, Folland CK, Alexander LV, Rowell DP (2003)  
393 Global analyses of sea surface temperature, sea ice, and night marine air temperature  
394 since the late nineteenth century. *J Geophys Res* 108(D14).

395 Saji NH, Goswami BN, Vinayachandran PN, Yamagata T (1999) A dipole mode in the  
396 tropical Indian Ocean. *Nature* 401(6751):360-363.

397 Schott FA, Dengler M, Schoenefeldt R (2002) The shallow overturning circulation of  
398 the Indian Ocean. *Prog Oceanogr* 53(1):57-103.

399 Sherin VR, Durand F, Gopalkrishna VV, Anuvinda S, Chaitanya AVS, Bourdallé-  
400 Badie R, Papa F (2018) Signature of Indian Ocean Dipole on the western boundary

401 current of the Bay of Bengal. Deep Sea Research Part I: Oceanographic Research  
402 Papers 136:91-106.

403 Stewart RH (2004) Introduction to Physical Oceanography. Prentice-Hall.

404 Wang WQ, Zhu XH, Wang CZ, Köhl A (2014) Deep Meridional Overturning  
405 Circulation in the Indian Ocean and Its Relation to Indian Ocean Dipole. J Climate  
406 27(12):4508-4520.

407 Webster PJ, Moore AM, Loschnigg JP, Leben RR (1999) Coupled ocean-atmosphere  
408 dynamics in the Indian Ocean during 1997-98. Nature 401(6751):356-360.

409 Xie SP, Annamalai H, Schott FA, McCreary JP (2002) Structure and Mechanisms of  
410 South Indian Ocean Climate Variability. J Climate 15(8):864-878.

411 Yang Y, Xie SP, Wu LX, Kosaka Y, Lau NC, Vecchi GA (2015) Seasonality and  
412 Predictability of the Indian Ocean Dipole Mode: ENSO Forcing and Internal Variability.  
413 J Climate 28(20):8021-8036.

414 Zhang YZ, Li JP, Xue JQ, Feng J, Wang QY, Xu YD, Wang YH, Zheng F (2018)  
415 Impact of the South China Sea Summer Monsoon on the Indian Ocean Dipole. J  
416 Climate 31(16):6557-6573.

417 Zhang YZ, Li JP, Xue JQ, Zheng F, Wu RG, Ha KJ, Feng J (2019) The relative roles  
418 of the South China Sea summer monsoon and ENSO in the Indian Ocean dipole  
419 development. Clim Dynam 53(11):6665-6680.

420

421

422

423

424

425

426

## 427 **Figure Captions**

428 **FIG. 1.** Positive IOD composites of wind stress anomaly (vectors; values larger than  
429  $0.01 \text{ N} \cdot \text{m}^{-2}$  are shown by bold arrows) and SST anomaly (shaded).

430 **FIG. 2.** Correlations of the DMI with wind stress (vector) and SST (shading) in autumn.  
431 Black stipples indicate the 99% confidence level. Only wind vectors that are significant  
432 at the 99% confidence level are plotted.

433 **FIG. 3.** (a) Correlation coefficients between the ZWI and the EETAI from MAM to  
434 DJF during 1958–2008. The dashed line indicates exceeding the 99% confidence level.  
435 (c) Standardized time series of the ZWI (blue line), the SON DMI (red line) and the  
436 SON EETAI (yellow line). The correlation coefficient  $R$  between them is  $-0.81$  ( $0.82$ ),  
437 beyond the 99% confidence level (Student's  $t$  test).

438 **FIG. 4.** Correlations of the ZWI with shallow streamfunction in autumn (shading).  
439 Black stipples indicate the 95% confidence level.

440 **FIG. 5.** (a) Correlations of the ZWI with Ekman transport (vector) and Ekman pumping  
441 (shading) in autumn. Black stipples indicate the 99% confidence level. Only Ekman  
442 transport that significant at the 99% confidence level are plotted. Ekman transport is  
443 not defined near the equator ( $2^{\circ}\text{S}$ - $2^{\circ}\text{N}$ ), where Ekman transport and Ekman pumping  
444 are not drawn. (b) Standardized time series of the ZWI (blue line), the SON DMI (red  
445 line) and the cross-equatorial Ekman transport (yellow line). The correlation coefficient  
446  $R$  between them is  $0.98$  ( $-0.77$ ), beyond the 99% confidence level (Student's  $t$  test).

447 **FIG. 6.** The Ekman transport (vectors; Sv) and Ekman pumping (shading) anomaly (a)  
448 of positive IOD composites and (b) of negative IOD composites. (c) The composite  
449 difference of the Ekman transport (vectors; Sv) and Ekman pumping (shading) of  
450 positive IOD and negative IOD. Black stipples indicate the 95% confidence level. Only  
451 vectors that are significant at the 95% confidence level are plotted.

452 **FIG. 7.** (a) The meridional seawater transport and (c) the shallow streamfunction  
453 anomaly of positive IOD composites. (b) The meridional seawater transport and (d) the  
454 shallow streamfunction anomaly of negative IOD composites. The composite  
455 difference of (e) the meridional seawater transport and (f) the shallow streamfunction  
456 of positive IOD and negative IOD. Solid stipples indicate the 90% confidence level. In  
457 (a), (b) and (e), the blue lines indicate Ekman transport, the orange lines stand for  
458 Sverdrup transport, and the red lines indicate the difference between Sverdrup transport  
459 and Ekman transport. In all subgraphs, the transverse axis represents latitude.

460 **FIG. 8.** Correlation of the ZWI with the surface ocean current (vector) in autumn. Only  
461 current vectors that are significant at the 95% confidence level are plotted.

462 **FIG. 9.** The surface ocean current anomaly (vectors; m/sec) of (a) positive IOD  
463 composites and (b) negative IOD composites. (c) The composite difference of the  
464 surface ocean current (vectors; m/sec) of positive IOD and negative IOD. Only current  
465 vectors that are significant at the 95% confidence level are plotted.

466 **FIG. 10.** (a) Regression of the shallow streamfunction on the ZWI. (b) Partial  
467 regression of the shallow streamfunction on the ZWI after removal of SON1 ENSO

468 signals. (c) Partial regression of the shallow streamfunction on the ZWI after removal  
469 of D1JF2 ENSO signals(D1JF2, where 1 and 2 refers to the concurrent and next year,  
470 respectively).Black stipples in (a) - (c) indicate the 95% confidence level.

471 **FIG. 11.** Schematic diagram of the equatorial wind stress affecting the equatorial  
472 Ekman transport in the positive phase of IOD. The blue shadow indicates the significant  
473 negative SSTAs, and red shadow indicates the positive SSTAs. The small black arrows  
474 represent the wind stress of the sea surface, the thick blue arrows represent Ekman  
475 transport, and the thin blue arrows represent the shallow MOC of the zonal integration.

476

477

478

479

480

481

482

483

484

485

486 **Table Captions**

487 **TABLE 1.** The partial correlation coefficients of the SON SMOCAI with the ZWI and  
488 the SON DMI during 1958 - 2008. The season in brackets denotes the averaged season  
489 of the different index, i.e., Rm-Niño3.4 (Pre-D0JF1/D1JF2) indicates the removal of  
490 the preceding/next boreal winter ENSO signals (D0JF1, D1JF2, where 0 refers to  
491 previous year, 1 refers to concurrent year and 2 refers to next year).

492

493

494

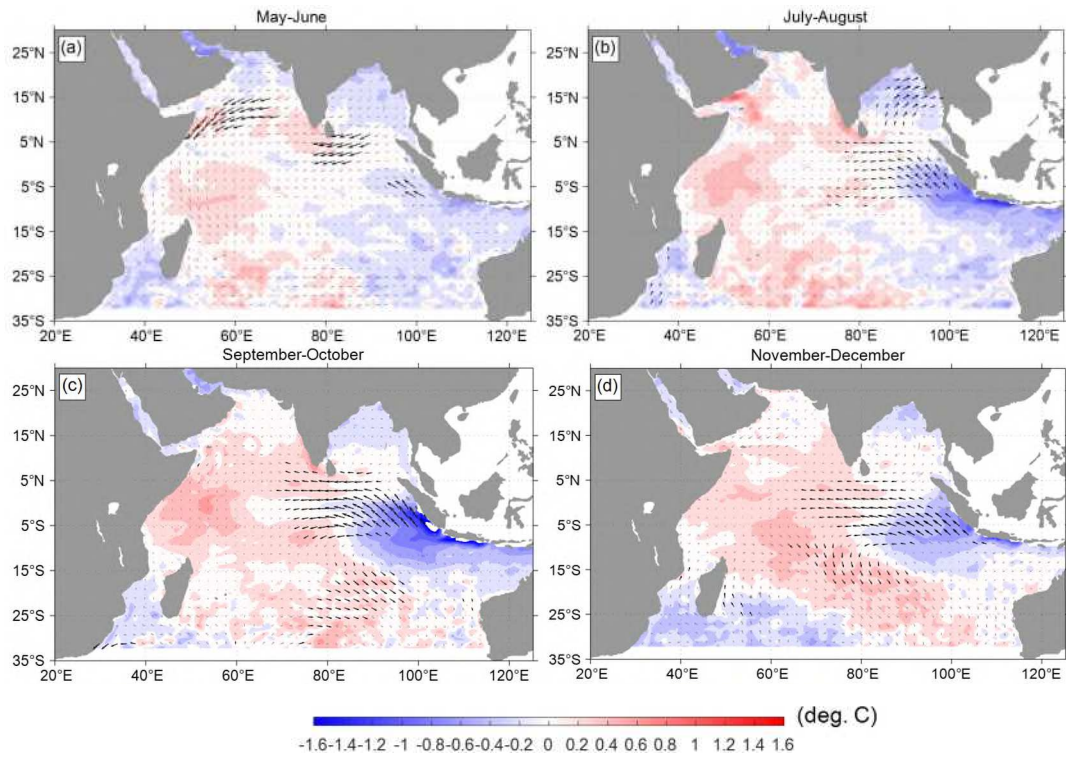
495

496

497

498

## Figures



500

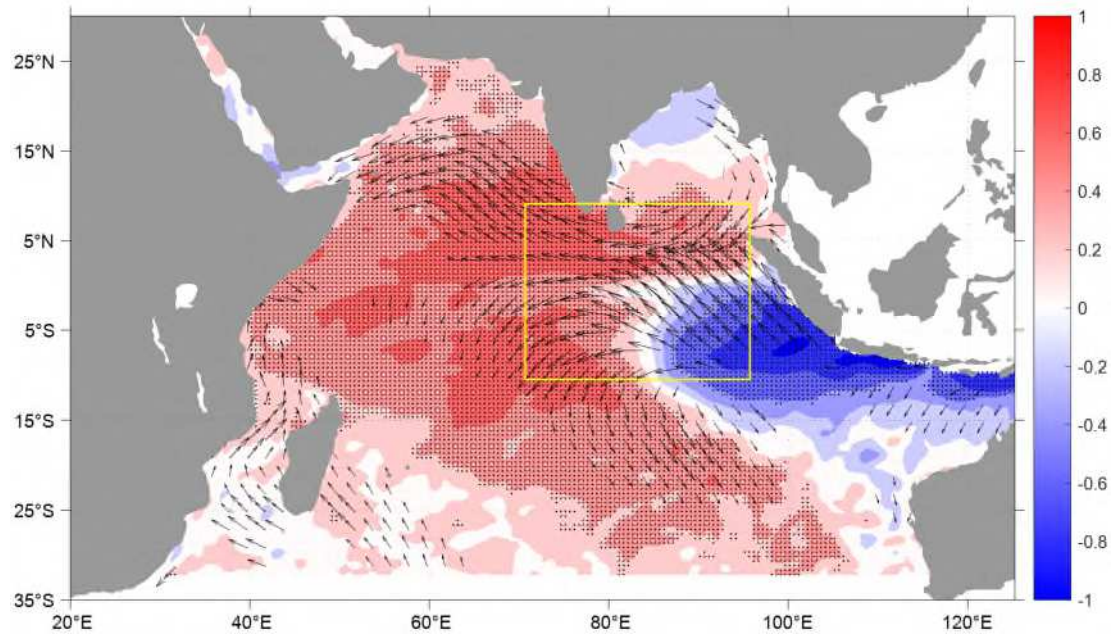
501 **FIG. 1.** Positive IOD composites of wind stress anomaly (vectors; values larger than502  $0.01 \text{ N}\cdot\text{m}^{-2}$  are shown by bold arrows) and SST anomaly (shaded).

503

504

505

506



507

508 **FIG. 2.** Correlations of the DMI with wind stress (vector) and SST (shading) in autumn.

509 Black stipples indicate the 99% confidence level. Only wind vectors that are significant

510 at the 99% confidence level are plotted.

511

512

513

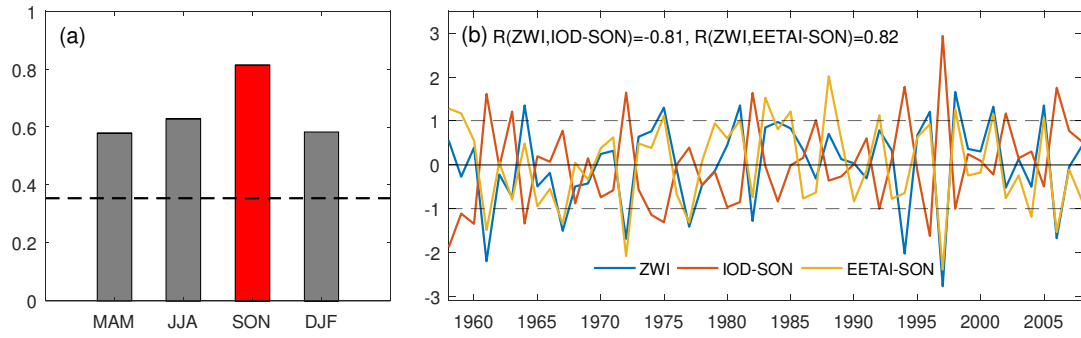
514

515

516

517

518



519

520 **FIG. 3** (a) Correlation coefficients between the ZWI and the EETAI from MAM to DJF  
 521 during 1958–2008. The dashed line indicates exceeding the 99% confidence level. (c)  
 522 Standardized time series of the ZWI (blue line), the SON DMI (red line) and the SON  
 523 EETAI (yellow line). The correlation coefficient  $R$  between them is  $-0.81$  ( $0.82$ ),  
 524 beyond the 99% confidence level (Student's  $t$  test).

525

526

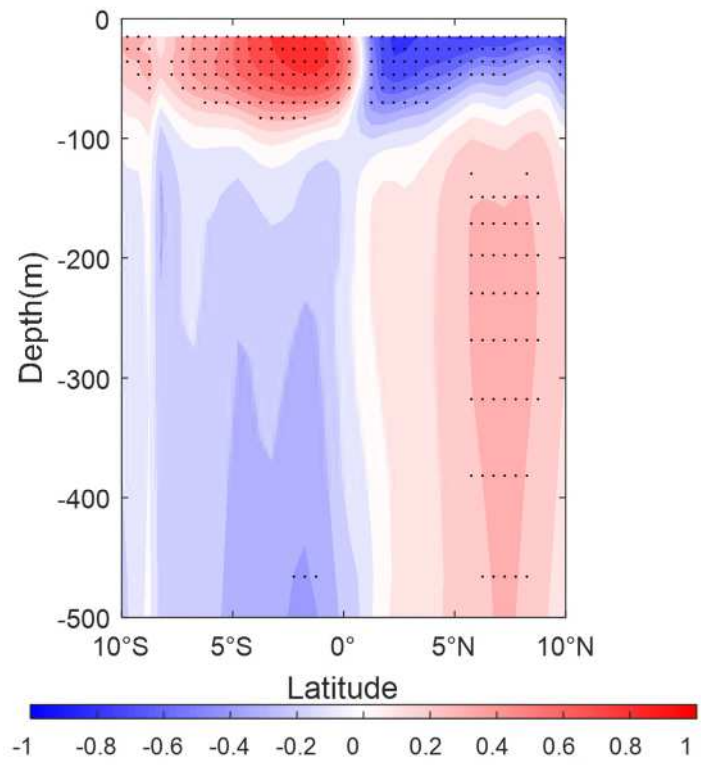
527

528

529

530

531



532

533 **FIG. 4.** Correlations of the ZWI with shallow streamfunction in autumn (shading).

534 Black stipples indicate the 95% confidence level.

535

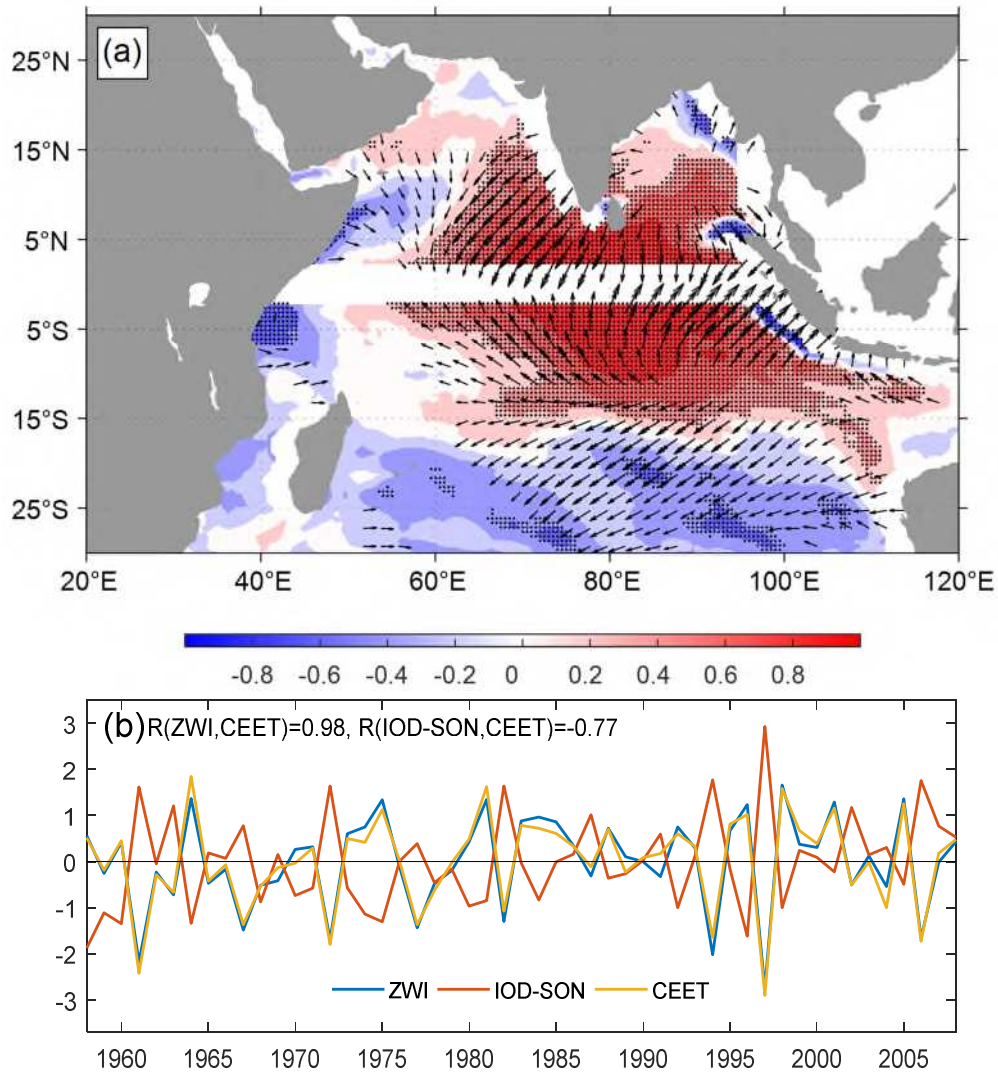
536

537

538

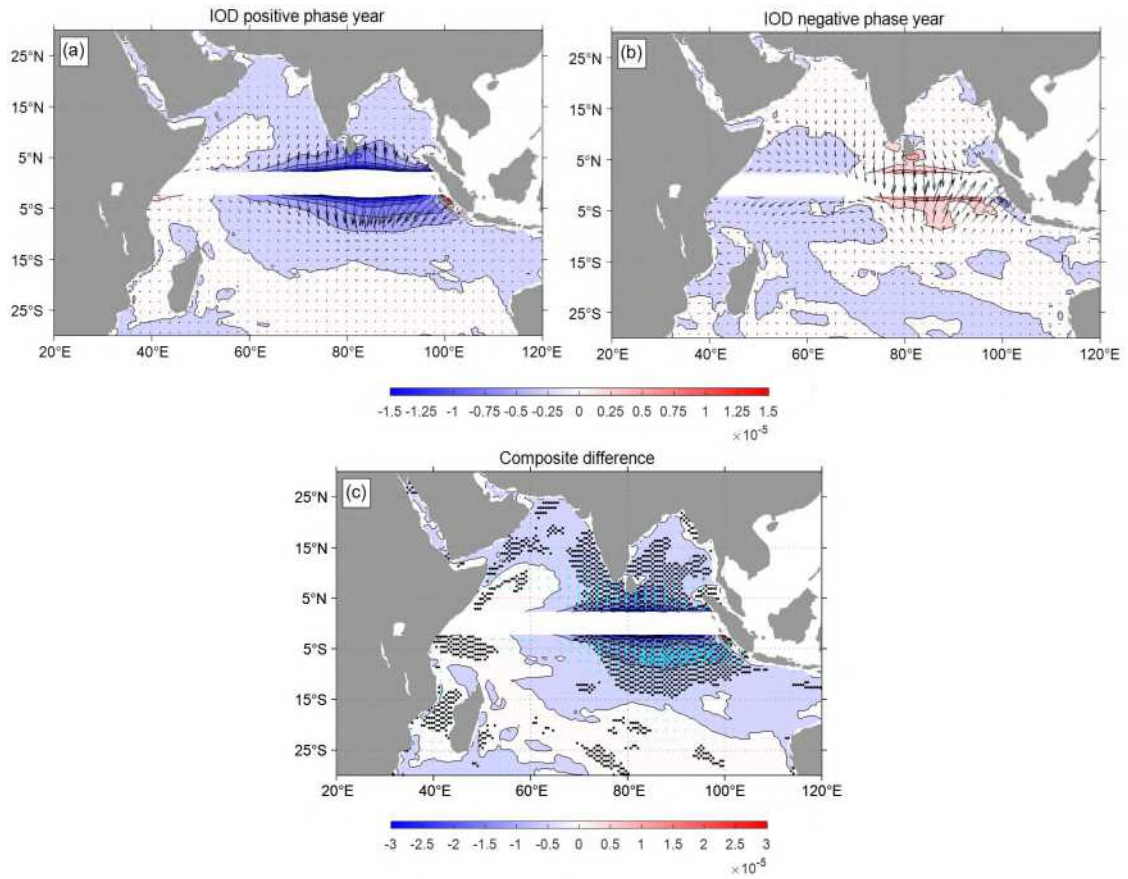
539

540



541

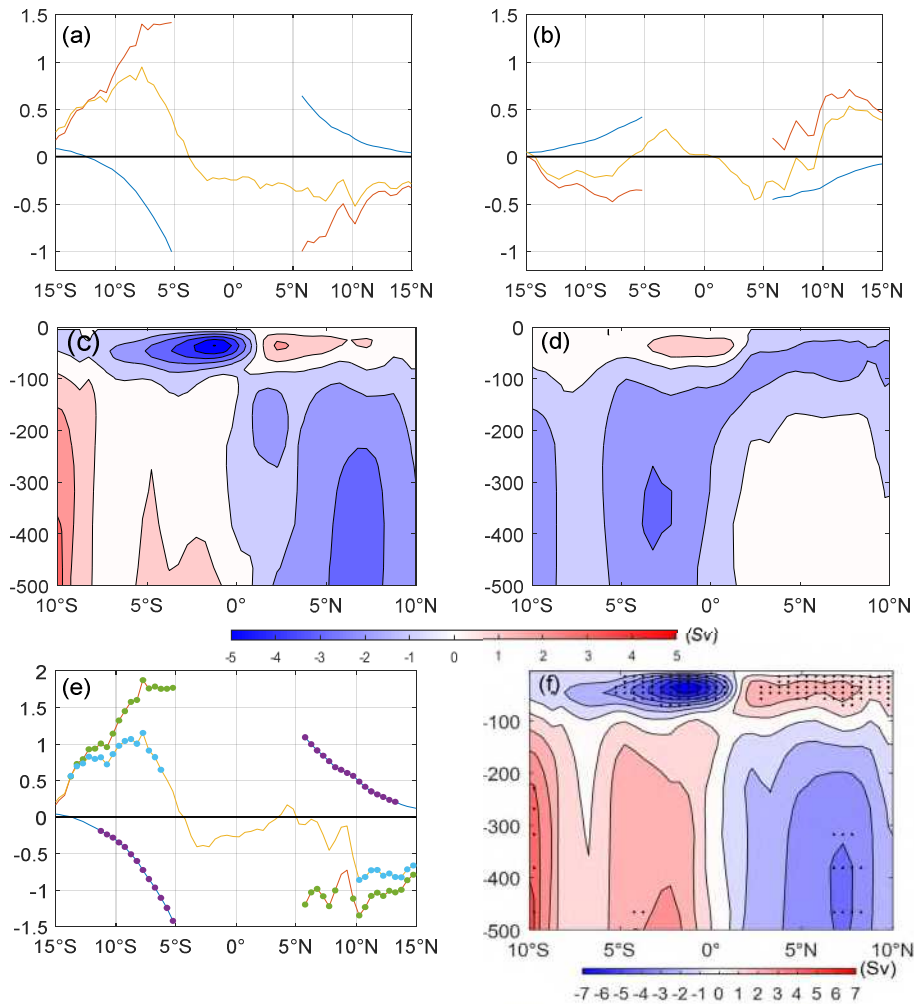
542 **FIG. 5.** (a) Correlations of the ZWI with Ekman transport (vector) and Ekman  
 543 pumping (shading) in autumn. Black stipples indicate the 99% confidence level. Only  
 544 Ekman transport that significant at the 99% confidence level are plotted. Ekman  
 545 transport is not defined near the equator (2°S-2°N), where Ekman transport and Ekman  
 546 pumping are not drawn. (b) Standardized time series of the ZWI (blue line), the SON  
 547 DMI (red line) and the cross-equatorial Ekman transport (yellow line). The correlation  
 548 coefficient  $R$  between them is 0.98 (-0.77), beyond the 99% confidence level (Student's  
 549  $t$  test).



550

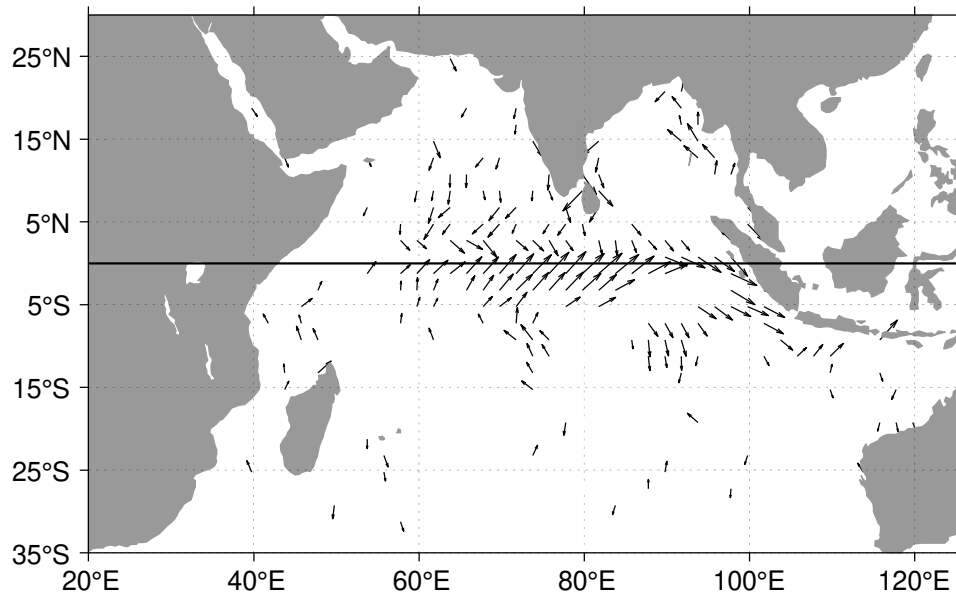
551 **FIG. 6.** The Ekman transport (vectors; Sv) and Ekman pumping (shading) anomaly (a)  
 552 of positive IOD composites and (b) of negative IOD composites. (c) The composite  
 553 difference of the Ekman transport (vectors; Sv) and Ekman pumping (shading) of  
 554 positive IOD and negative IOD. Black stipples indicate the 95% confidence level. Only  
 555 vectors that are significant at the 95% confidence level are plotted.

556



557

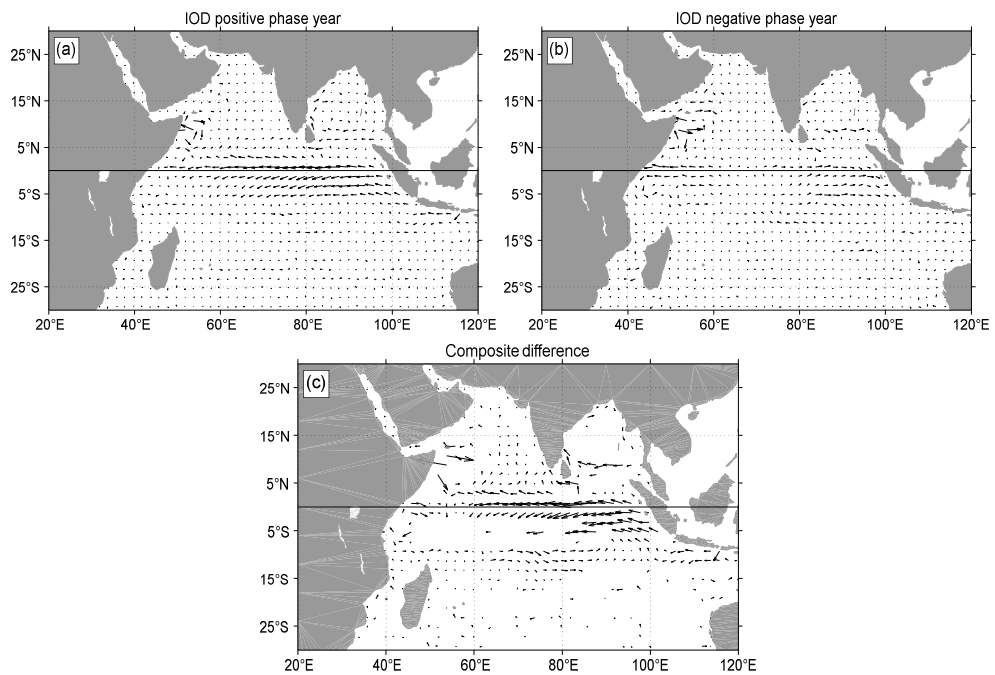
558 **FIG. 7.** (a) The meridional seawater transport and (c) the shallow streamfunction  
 559 anomaly of positive IOD composites. (b) The meridional seawater transport and (d) the  
 560 shallow streamfunction anomaly of negative IOD composites. The composite  
 561 difference of (e) the meridional seawater transport and (f) the shallow streamfunction  
 562 of positive IOD and negative IOD. Solid stipples indicate the 90% confidence level. In  
 563 (a), (b) and (e), the blue lines indicate Ekman transport, the orange lines stand for  
 564 Sverdrup transport, and the red lines indicate the difference between Sverdrup transport  
 565 and Ekman transport. In all subgraphs, the transverse axis represents latitude.



566

567 **FIG. 8.** Correlation of the ZWI with the surface ocean current (vector) in autumn.

568 Only current vectors that are significant at the 95% confidence level are plotted.



569

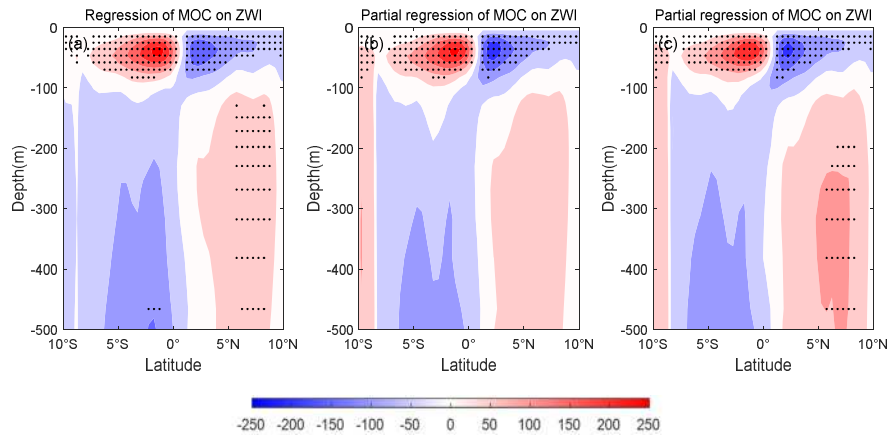
570 **FIG. 9.** The surface ocean current anomaly (vectors; m/sec) of (a) positive IOD  
 571 composites and (b) negative IOD composites. (c) The composite difference of the  
 572 surface ocean current (vectors; m/sec) of positive IOD and negative IOD. Only current  
 573 vectors that are significant at the 95% confidence level are plotted.

574

575

576

577



578

579 **FIG. 10.** (a) Regression of the shallow streamfunction on the ZWI. (b) Partial  
 580 regression of the shallow streamfunction on the ZWI after removal of SON1 ENSO  
 581 signals. (c) Partial regression of the shallow streamfunction on the ZWI after removal  
 582 of D1JF2 ENSO signals(D1JF2, where 1 and 2 refers to the concurrent and next year,  
 583 respectively).Black stipples in (a) – (c) indicate the 95% confidence level.

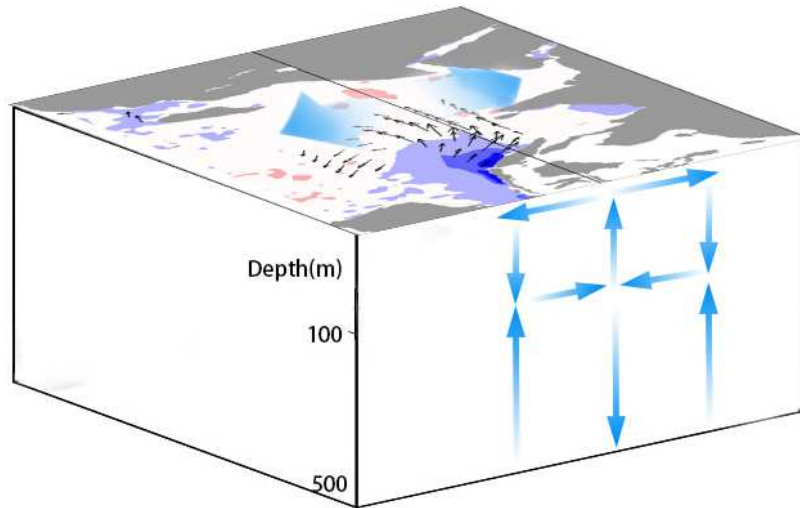
584

585

586

587

588



589

590 **FIG. 11.** Schematic diagram of the equatorial wind stress affecting the equatorial  
 591 Ekman transport in the positive phase of IOD. The blue shadow indicates the significant  
 592 negative SSTAs, and red shadow indicates the positive SSTAs. The small black arrows  
 593 represent the wind stress of the sea surface, the thick blue arrows represent Ekman  
 594 transport, and the thin blue arrows represent the shallow MOC of the zonal integration.

595

596

597

598

599

600

601

602

603 **TABLE 1.** The partial correlation coefficients of the SON EETAI with the ZWI and the  
604 SON DMI during 1958 – 2008. The season in brackets denotes the averaged season of  
605 the different index, i.e., Rm-Niño3.4 (Pre-D0JF1/D1JF2) indicates the removal of the  
606 preceding/next boreal winter ENSO signals (D0JF1, D1JF2, where 0 refers to previous  
607 year, 1 refers to concurrent year and 2 refers to next year).

	correlation	Partial correlation				
		Rm-Nino-3.4 (Pre-D0JF1)	Rm-Nino-3.4 (Pre-MAM1)	Rm-Nino-3.4 (Pre-JJA1)	Rm-Nino-3.4 (SON1)	Rm-Nino-3.4 (Pre-D1JF2)
(ZWI, SON-EETAI)	0.82	0.81	0.82	0.72	0.69	0.72
(SON-DMI, SON-EETAI)	-0.79	-0.78	-0.79	-0.67	-0.64	-0.70

608